



Research Paper

# DYNAMIC ANALYSIS OF COMPLIANT BASED PSEUDO-RIGID-BODY CONSTANT FORCE SLIDER CRANK MECHANISM USING THE ENVIRONMENT LIKE ANSYS

Amit Gupta<sup>1\*</sup>, S S Rattan<sup>1</sup> and Sudipto Mukherjee<sup>2</sup>

\*Corresponding Author: **Amit Gupta**, ✉ [amitgupta4u@rediffmail.com](mailto:amitgupta4u@rediffmail.com)

A mathematical dynamic model is derived for the compliant constant-force mechanism, based on the pseudo-rigid-body model simplification of the device. The compliant constant-force mechanism is a slider mechanism incorporating large-deflection beams, which outputs near-constant-force across the range of its designed deflection. The equation of motion is successfully validated with empirical data. The dynamic model is cast for one out of 28 possible configurations of compliant constant-force slider crank mechanism, identified by type synthesis techniques (Howell, 2001). The author derived the dynamic model through Lagrange's Equation for the selected configuration of compliant constant-force slider crank mechanism. An unexpected dynamic trait of the constant-force mechanism is discovered: there exists a range of frequencies for which the output force of the mechanism accords nearer to constant-force than does the output force at static levels.

**Keywords:** Compliant mechanism, Pseudo rigid body slider crank mechanism, Constant force mechanism

## INTRODUCTION

### Compliant Joint or Flexure Hinge

A flexure hinge is a thin member that provides the relative rotation between two adjacent rigid members through flexing (bending). However, the clearance between mating parts of rigid conventional joints causes backlash in

mechanical assemblies. Further, in all the above joints there is relative motion causing friction that leads to wear and increased clearances. A kinematic chain of such joints compounds the individual errors from backlash and wear, resulting in poor accuracy and repeatability.

<sup>1</sup> Department of Mechanical Engineering, NIT, Kurukshetra 136119, India.

<sup>2</sup> Department of Mechanical Engineering, IIT, Delhi, India.

**Figure 1: Compliant Joint**



**Figure 2: Conventional Joint**



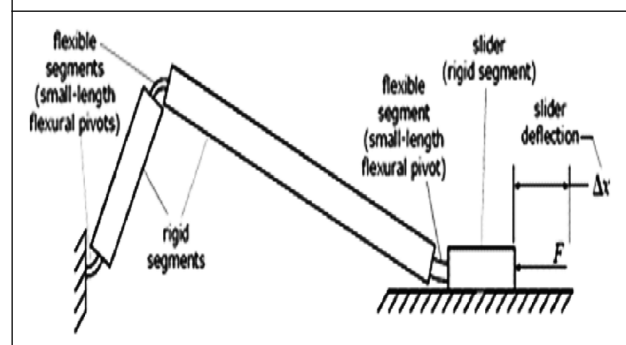
**Compliant Mechanisms and The Pseudo-Rigid-Body Model**

The emergence of the pseudo-rigid-body model in recent years coincides with the building realization of the aptness of compliance in engineering. Natural world also reveals the strength of compliance, such as the flexible wings of a bee or hummingbird, or the versatility of the human hand and wrist (Vogel, 1995). However, nature is difficult to mimic because of the complex nonlinear analysis required to understand all but small-deflection compliance. The pseudo-rigid-body model is a method of circumventing some of the obstacles that arise when engineering compliance into mechanical devices. It provides a welcome middle ground between designing merely by trial and error, and devising exact mathematical formulations.

**Compliant Constant-Force Mechanisms**

A constant-force mechanism yields a constant output force over a range of input displacements. Compliant constant-force mechanisms are essentially compliant slider mechanisms with flexible and rigid segment dimensions optimized to minimize the variation in the output force over a designed range of displacement. Consider the compliant slider mechanism depicted in Figure. Given an input displacement  $\Delta x$ , a compliant constant-force mechanism will yield the same force  $F$  over the full range of its designed deflection, plus or minus a small variation.

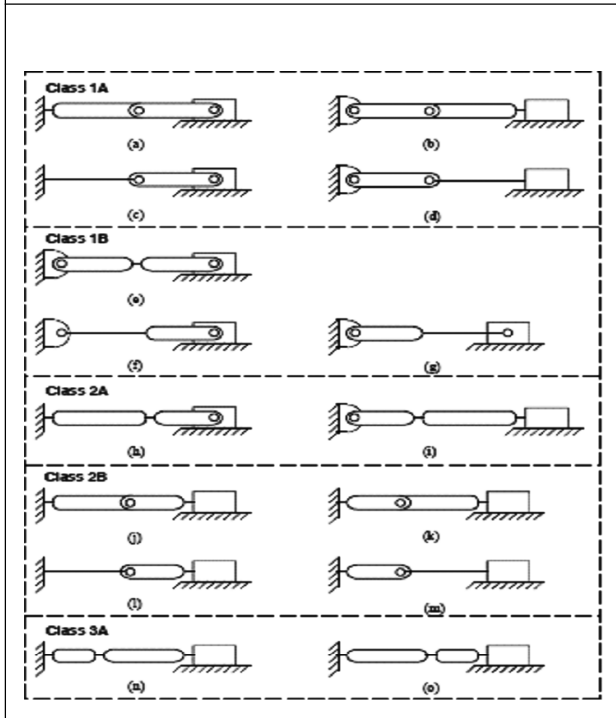
**Figure 3: Compliant Slider Mechanism**



There exist 28 possible configurations of the compliant constant-force mechanism, identified by type synthesis techniques (Howell, 2001). Of these, fifteen configurations are illustrated in Figure (Millar *et al.*, 1996). Experimental validation of dynamic models of one of these configurations is performed in this paper.

The pseudo-rigid-body model approximates the deflection and force characteristics of a complaint mechanism's flexible members by assigning them torsional spring and rigid-link counterparts. Applying the model to the entire compliant mechanism

**Figure 4: Fifteen Configurations of the Compliant Constant-Force Mechanism Flexible Segments are Depicted by a Single Line, and Rigid Segments are Depicted by Two Parallel Lines**

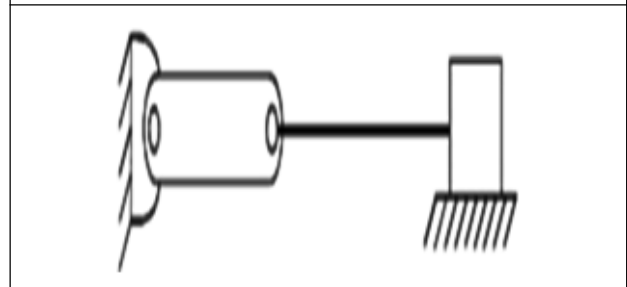


using a series of heuristic rules results in a rigid-link model. Herein lies the power of the pseudo-rigid-body model: its ability to convert a difficult-to-analyze compliant mechanism into a familiar rigid-body mechanism which can be analyzed using traditional kinematics. The model does not represent compliant mechanisms perfectly, but it has been shown to represent them very well, making it a powerful design tool. Though the pseudo-rigid-body model has been shown to be valid for the static analysis of compliant mechanisms, very little research has been performed to explore the usefulness of the pseudo-rigid-body model in dynamic analysis. If the model can be shown to approximate well the dynamic response of compliant mechanisms, then its usefulness is extended even further.

### Dynamic Model

The derivation of a closed-form dynamic model for constant-force mechanism configuration “Class 1A-d,” as designated in [Figure](#).

**Figure 5: Compliant Constant-Force Mechanism, Configuration Class 1A-d**

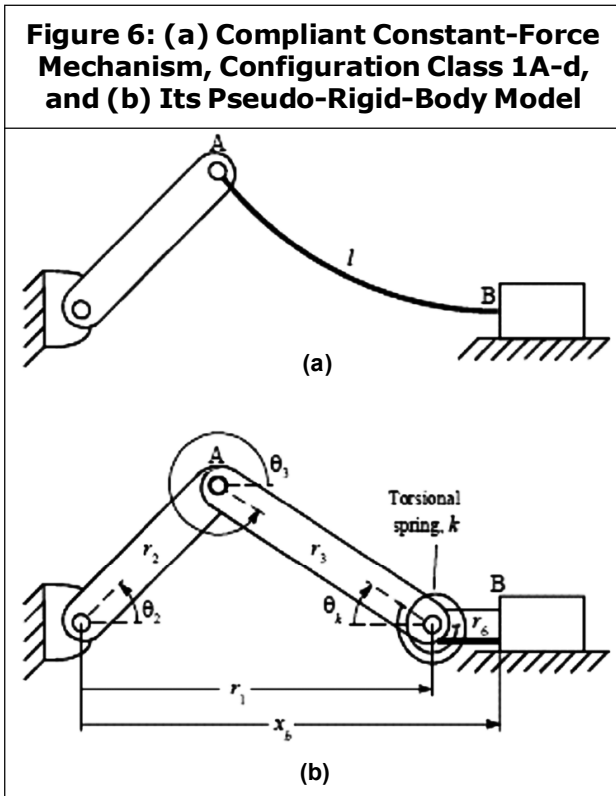


First, the compliant mechanism is modeled as a rigid-body mechanism with lumped compliance using the pseudo-rigid-body model. Converting the mechanism to its rigid-body counterpart greatly simplifies kinematic and dynamic analysis by allowing the use of rigid-body modeling techniques. Lagrange’s method is then used to obtain an equation of motion for the mechanism. The constant-force mechanism has only one degree of freedom, so only one generalized coordinate and one instance of Lagrange’s equation are required. The choice of non-conservative forces included in the generalized force is explained, as well as any assumptions made by the model.

The mechanism is converted to its rigid-body counterpart by using the pseudo-rigid-body model rule for a cantilever beam with a force at the free end as described below.

The flexible segment of length  $l$  is replaced by two rigid links, links 3 and 6, with lengths  $r_3$  and  $r_6$ . Link 3’s length is determined by the relation for the pseudo-rigid-body link’s characteristic radius,  $r_3 = \gamma l$ , where  $\gamma$  is the

characteristic radius factor. The length of link 6 is then  $r_6 = l - r_3$ . The compliance of the flexible segment is represented by a torsional spring at the new pin (“characteristic pivot”) joining links 3 and 6. The torsional spring constant  $k$  for a cantilever beam with a force at the free end is given by  $K = \gamma K_0 E I l$ .



where  $K_0$  is the stiffness coefficient (a nondimensionalized torsional spring constant),  $E$  is the modulus of elasticity of the flexible segment, and  $I$  is the moment of inertia of the flexible segment. The average values of  $\gamma$  and  $K_0$  over a wide range of loading conditions are used:  $\gamma = 0.85$ ,  $K_0 = 2.65$

For a more accurate  $k$  that changes with deflection of the flexible segment,  $\gamma$  and  $K_0$  can be expressed as functions of end-load angle, but equation gives the average values most commonly used in pseudo-rigid-body model calculations.

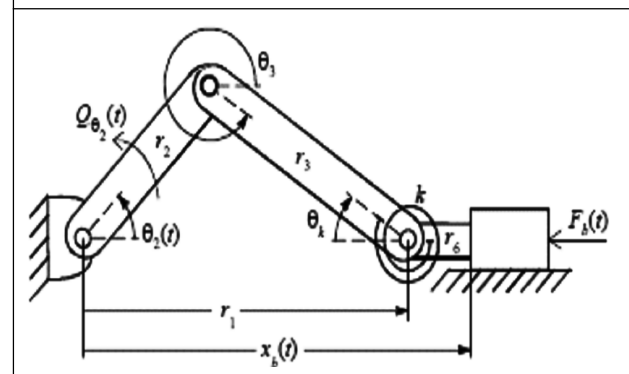
When the pseudo-rigid-body angle  $\theta_k$  is zero, the torsional spring is undeflected and stores no strain energy. It is assumed that no plastic deformation occurs as the mechanism cycles and the flexible segment deflects.

**Formulating the Lagrangian**

Given an input slider displacement  $x_b(t)$ , the dynamic model should indicate the reaction force  $F_b(t)$  at the slider. The independent coordinate  $x_b(t)$  could be chosen as the generalized coordinate for Lagrange’s equation and would result in a generalized force corresponding to  $F_b(t)$ . Instead  $\theta_2(t)$  will be chosen as the generalized coordinate, corresponding to a generalized force  $Q_{\theta_2}(t)$ . Choosing  $\theta_2$  as the generalized coordinate simplifies much of the derivation. Note that because  $\theta_2$  is an angle, the generalized force  $Q_{\theta_2}$  has units of moment; a relation to transform between  $Q_{\theta_2}$  and  $F_b$  will be given at the end.

The Lagrangian  $L$  is formed by taking the difference of the scalar quantities of kinetic energy  $T$  and potential energy  $V$  of the system,  $L = T - V$ .

**Figure 7: Reaction Force  $F_b(t)$  at the Slider (Output Port); Independent Generalized Coordinate  $\theta_2(t)$  and Generalized Force  $Q_{\theta_2}(t)$**



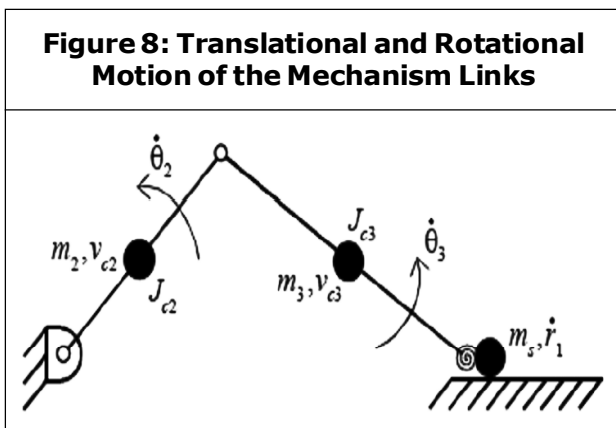
One way to formulate  $T$  is to separate the motion of the mechanism inertias into both

translation and rotation. The center of mass of each link translates along a predefined path as the mechanism moves, and each link rotates about its center of mass. The mass of link 6 can be lumped together with the mass of the slider since both travel along a linear path and neither rotates:  $m_s = m_6 + m_{slider}$ .

The first three terms of the kinetic energy expression represent the translational energy of the system, and the last two represent the rotational energy:

$$T = \frac{1}{2} m_2 (v_{c2})^2 + \frac{1}{2} m_3 (v_{c3})^2 + \frac{1}{2} m_s (r_1)^2 + \frac{1}{2} J_{c2} (\dot{\theta}_2)^2 + \frac{1}{2} J_{c3} (\dot{\theta}_3)^2$$

where  $m_i$  is the mass,  $v_{ci}$  is the velocity of the center of mass,  $J_{ci}$  is the mass moment of inertia, and  $\dot{\theta}_i$  is the angular velocity of links 2 and 3;  $r_1$  is the velocity of the slider.



The mass moments of inertia of links 2 and 3 are:

$$J_{ci} = \frac{1}{12} m_i r_i^2$$

Assuming the mechanism lies in a plane perpendicular to gravity, the potential energy of the system is simply the torsional spring energy.

$$V = \frac{1}{2} K \theta_k^2$$

The Lagrangian  $L = T - V$  must be expressed in terms of the generalized coordinate  $\theta_2$  and its time derivative  $\dot{\theta}_2$  before forming Lagrange's equation. The following equations recast the variables in  $T$  and  $V$  in terms of  $\theta_2$  and  $\dot{\theta}_2$

$$V_{c2}^2 = \frac{1}{4} r_2^2 \dot{\theta}_2^2$$

$$V_{c3}^2 = r_2^2 \dot{\theta}_2^2 + \frac{1}{4} r_3^2 \dot{\theta}_3^2 + r_2 r_3 \cos(\theta_2 - \theta_3) \dot{\theta}_2 \dot{\theta}_3$$

$$\dot{r}_1^2 = [r_2 \sin \theta_2 \dot{\theta}_2 + r_3 \sin \theta_3 \dot{\theta}_3]^2$$

$$\theta_k = a \sin\left(\frac{r_2}{r_3} \sin \theta_2\right)$$

$$\theta_3 = a \sin\left(\frac{r_2}{r_3} \sin \theta_2\right)$$

$$\dot{\theta}_3 = \frac{r_2 \cos \theta_2}{\sqrt{r_3^2 - r_2^2 \sin^2 \theta_2}}$$

It is also useful to give  $x_b$  as a function of  $\theta_2$ :

$$x_b = r_1 + r_6$$

where,

$$r_1 = r_2 \cos \theta_2 + \sqrt{r_3^2 - r_2^2 \sin^2 \theta_2}$$

### Lagrange's Equation

Using Lagrange's formulation, the equation of motion for the system is expressed as

$$\frac{d}{dt} \left( \frac{\partial L}{\partial \dot{\theta}_2} \right) - \frac{\partial L}{\partial \theta_2} = Q_{\theta_2}$$

The left side of the equation is a statement of the principle of conservation of energy, and

the right side represents the non-conservative generalized force (Thomson and Dahleh, 1998). When the derivatives of the Lagrangian are expanded out, the equation of motion for the system becomes

$$\left[ m_3 \left( \frac{1}{2} \frac{r_2^5 \sin^3 \theta_2 \cos^2 \theta_2}{\xi^2} + \frac{1}{3} \frac{r_2^4 r_3^2 \sin \theta_2 \cos^3 \theta_2}{\xi^2} - \frac{1}{2} \frac{r_2^3 \sin^3 \theta_2}{\sqrt{\xi}} + \frac{r_2^3 \sin \theta_2 \cos^2 \theta_2}{\sqrt{\xi}} - \frac{1}{3} \frac{r_2^2 r_3^2 \sin \theta_2 \cos \theta_2}{\xi} + r_2^2 \sin \theta_2 \cos \theta_2 \right) + m_s \left( \frac{r_2^6 \sin^3 \theta_2 \cos^3 \theta_2}{\xi^2} + \frac{r_2^5 \sin^3 \theta_2 \cos^2 \theta_2}{\xi^2} - \frac{r_2^4 \sin^3 \theta_2 \cos \theta_2}{\xi} + \frac{r_2^4 \sin \theta_2 \cos^3 \theta_2}{\xi} + 2 \frac{r_2^3 \sin \theta_2 \cos^2 \theta_2}{\sqrt{\xi}} - \frac{r_2^3 \sin^3 \theta_2}{\sqrt{\xi}} + r_2^2 \sin \theta_2 \cos \theta_2 \right) \right] \dot{\theta}_2^2 + \left[ m_2 \left( \frac{1}{3} r_2^2 \right) + m_3 \left( \frac{r_2^3 \sin^2 \theta_2 \cos \theta_2}{\sqrt{\xi}} + \frac{1}{3} \frac{r_2^2 r_3^2 \cos^2 \theta_2}{\xi} + r_2^2 - r_2^2 \cos^2 \theta_2 \right) + m_s \left( \frac{r_2^4 \sin^2 \theta_2 \cos^2 \theta_2}{\xi} + 2 \frac{r_2^3 \sin^2 \theta_2 \cos \theta_2}{\sqrt{\xi}} + r_2^2 \sin^2 \theta_2 \right) \right] \ddot{\theta}_2 + k \frac{\sin \left( \frac{r_2}{r_3} \sin \theta_2 \right) r_2 \cos \theta_2}{\sqrt{\xi}} = Q_{\theta_2}$$

where

$$\xi = r_3^2 - r_2^2 \sin^2 \theta_2$$

The generalized force  $Q_{\theta_2}$  consists of a moment due directly to the force  $F_b$  acting on the slider  $\tau_{F_b}$ , a torque due to Coulomb pin friction  $\tau_c$ , and a term to compensate for unmodeled torque in the mechanism  $\tau_{\mu m}$ :

$$Q_{\theta_2} = \tau_{F_b} + \tau_c + \tau_{\mu m}$$

Though more elaborate expressions for the Coulomb friction term  $\tau_c$  are possible, the following simple relation gives sound results

$$\tau_c C \theta_2 \sin(\dot{\theta}_2)$$

Multiplying by  $\theta_2$  is a departure from classical Coulomb friction formulation, but it gives better results, and is based on the idea that the classical Coulomb friction coefficient is likely to be proportional to the angle  $\theta_2$ .

The values of the Coulomb friction coefficient  $C$  and the unmodeled torque  $\tau_{\mu m}$  are chosen using experimental data from static tests, as described in the next section.

Finally, to transform from the torque  $\tau_{F_b}$  to the mechanism's output force  $F_b$ , use the expression

$$F_b = \frac{\tau_{F_b}}{\frac{\partial x_b}{\partial \theta_2}}$$

where,

$$\frac{\partial x_b}{\partial \theta_2} = -r_2 \sin \theta_2 - \frac{r_2^2 \sin \theta_2 \cos \theta_2}{\sqrt{\xi}}$$

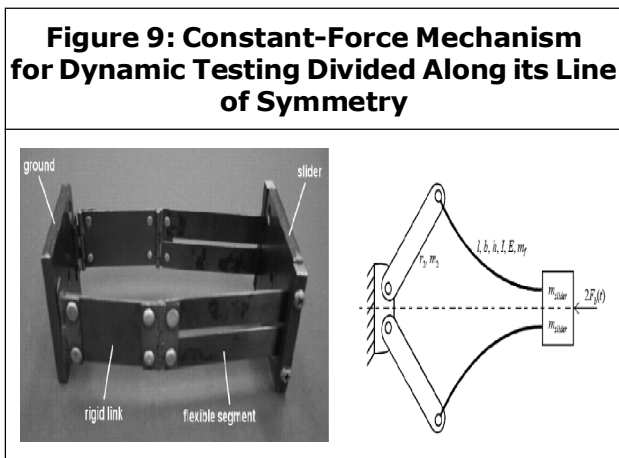
### Experimental Setup

To test the validity of the dynamic model, a constant-force test mechanism Class 1A-d constant-force mechanisms mounted to the same ground and sharing the same slider. Mounting two mechanisms opposite each other is useful because each cancels the moment induced by the other, and the issue of friction between slider and ground is eliminated.

To apply the dynamic model to the pair of constant-force springs, simply imagine the

device split down its line of symmetry. The parameters of one of the halves (i.e., link lengths, masses, etc.), are used in the dynamic model equations to solve for the predicted force  $F_b(t)$  of a single mechanism. The force expected at the output port of the constant-force spring pair is then twice  $F_b(t)$ . Note that the value of  $m_{slider}$  is half the mass of the shared slider, not its entire mass.

Each rigid link of the test mechanism is made of 1.19 mm-thick steel sheet metal, and each flexible segment is made of two strips of 0.64 mm-thick steel shim stock. Utility hinges serve as pins between ground and each rigid link, and between each rigid link and flexible segment. Both ground pins mount to a steel ground plate, and both flexible segments clamp to the shared slider, another steel plate.



The relevant dimensions, masses (incorporating the masses of the hinges and clamps), and properties of the test mechanism are listed in Table. Parameters used directly in the dynamic model equations are emphasized. The variables  $b$ ,  $h$ , and  $I$  are the width, thickness, and area moment of inertia of the flexible segment's cross section;  $E$  and  $m_f$  are the modulus of elasticity and mass of the flexible segment. The test mechanism was

designed to exhibit constant-force for a maximum of 40% deflection, or a deflection of  $\Delta x_b = 0.40(r_2 + r_3)$ , or 4.757 cm. The mechanism's total extended length is  $r_2 + l$ , or 13.007 cm.

The device's nominal constant-force  $F_{nom}$  (doubled for the mechanism pair), as derived in Howell (2001) is

$$F_{nom} = 2 \frac{k}{r_3} \varphi = 50.19 \text{ N}$$

The average non-dimensionalized constant-force  $\Phi$  for a 40% deflection Class 1A constant-force mechanism, tabulated in Millar et al. (1996), is  $\Phi = 0.4773$ .

Figure 9 shows a photograph of the experimental setup used to validate the constant-force mechanism dynamic model. The setup was designed to allow testing of the mechanism by sinusoidally cycling it (through compression and expansion) at different frequencies. Comparing the force data obtained from these tests with the force predicted by the dynamic model will authenticate or invalidate the model. The experimental setup is described here.

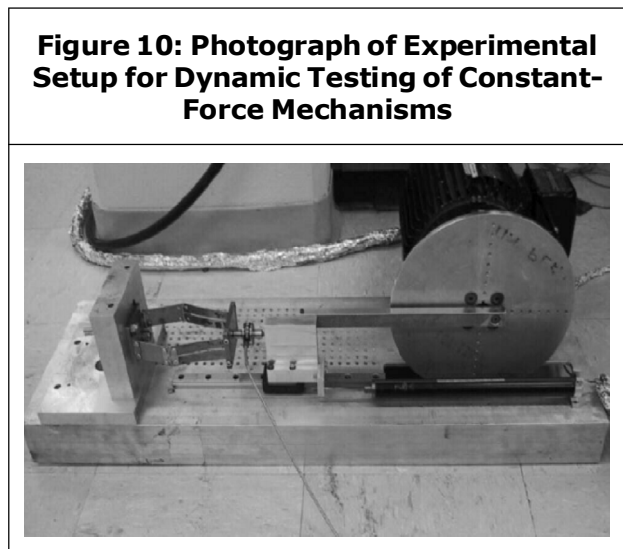


**Table 1: Test Mechanism Dimensions, Material Properties, and Masses (Parameters Used Directly in Dynamic Model Equations)**

Parameter	Value	Parameter	Value
$r^2$	5.490 cm	$I = bh^3/12$	$5.420 \times 10^{-13} \times m^4$
$l$	7.517 cm	$E$	206.8 GPa
$r_3 = \gamma l$	6.390 cm	$m_2$	13.8 g
$r_6 = l - r_3$	1.128 cm	$m_f$	10.7 g
$b$	2.540 cm	$m_3 = \gamma m_f$	9.1 g
$h$	0.064 cm	$m_6 = m_f - m_3$	1.6 g
$m_{slider}$	84.7 g	$K$	3.359 N-m
$m_s = m_{slider} + m_6$	86.3 g	$C$	0.055 N-m
$\tau_{,m}$	-0.235 N-m		

The constant-force test mechanism detailed in the proceeding section bolts to a thick aluminum ground, mounted perpendicular to a large aluminum table. In this manner both ground pins of the test mechanism are fixed with respect to the Table 1.

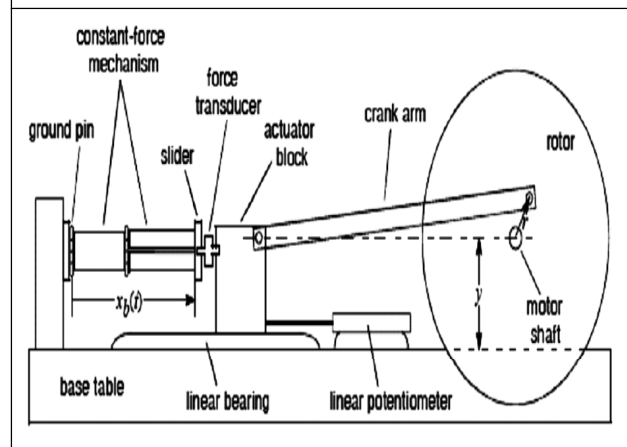
The test mechanism slider is actuated by a small aluminum block free to move across a linear bearing. Driving the actuator block is a velocity-controlled 2-hp motor with a rotor and crank-arm. The center of the motor shaft and the point of attachment of the crank-arm to the actuator block share the same height  $y$  from base table, as depicted in Figure. As such, assuming constant angular velocity of the motor and a small crank radius  $r$ , the actuator block drives the mechanism with an approximately sinusoidal velocity.

The rotor is drilled with a series of tapped holes, each located at a different radius, for variable positioning of the crank arm. This allows for larger or smaller total linear displacements of the mechanism as the rotor cycles.

Bolted in-line between the actuator block and test mechanism, a load cell measures

force exerted on the slider. Half of the mass of the load cell is lumped with the test mechanism's slider. The instrument used is a strain-gauge force transducer. Force measurement errors due to unwanted torque from the load cell's placement between the actuator block and slider were found to be less than 0.311 N, and so deemed to be negligible.

**Figure 11: Line Diagram of Experimental Setup**



A linear potentiometer measures mechanism deflection. The potentiometer housing is mounted to the base table, with its positioning rod attached to the actuator block. Since the actuator block, load cell, and slider are bolted together, the potentiometer measures the position  $x_b(t)$ , a measurement of the point where mechanism meets the slider, located with respect to where the mechanism attaches to ground. Both force and position data were acquired through a Measurement and Instrumentation lab of Rawal Institute of Engineering and Technology Faridabad.

This setup allows for the testing of the constant-force mechanism prototype over a range of frequencies, up to about 85 rad/s, above which there is danger of harming the setup equipment and/or the mechanism.

## Dynamic and Static Testing

Both dynamic and static tests can be performed using the experimental setup described above. Dynamic tests are performed by setting the motor controller to run at a constant velocity, waiting for the system to reach steady-state, then collecting data at a sampling rate well above the input sinusoid frequency. The position of the mechanism mount is adjusted so that at maximum expansion the mechanism has a preload.

Static tests are performed by removing the crank arm from the setup and again preloading the mechanism, this time using a long bar clamp. The clamp is slowly screwed tight compressing the mechanism, and then unscrewed allowing it to expand back to its initial position. Depending on whether the test is dynamic or static, the data is processed differently.

## Dynamic Data Processing

Unlike a static test, a dynamic test must be performed with the motor running, which introduces a sizable amount of electrical interference. To eliminate electrical noise from the data, both position and force signals are low-pass filtered through an 8<sup>th</sup>-order Butterworth filter with a cutoff frequency of 314 rad/s.

As previously explained, for every dynamic test the input position  $x_b(t)$  is always constrained to be a sinusoid. The mechanism's force output during one cycle, from its expanded state through compression and back to expansion, at any frequency. To cancel measurement errors from cycle to cycle in a given data set and to condense the data for ease of viewing, 30 force cycles are averaged together.

## Static Data Processing

Since a static test does not require the motor to be on, no filtering of electrical noise is necessary. Also, because a static test consists of only one cycle, no averaging is required. Position and force signals for static tests were both found to be clean, reliable, and free of noise, so the data was used as collected.

In every plot that displays measured force data (whether dynamic or static), spacing between plotted points is the time interval between samples.

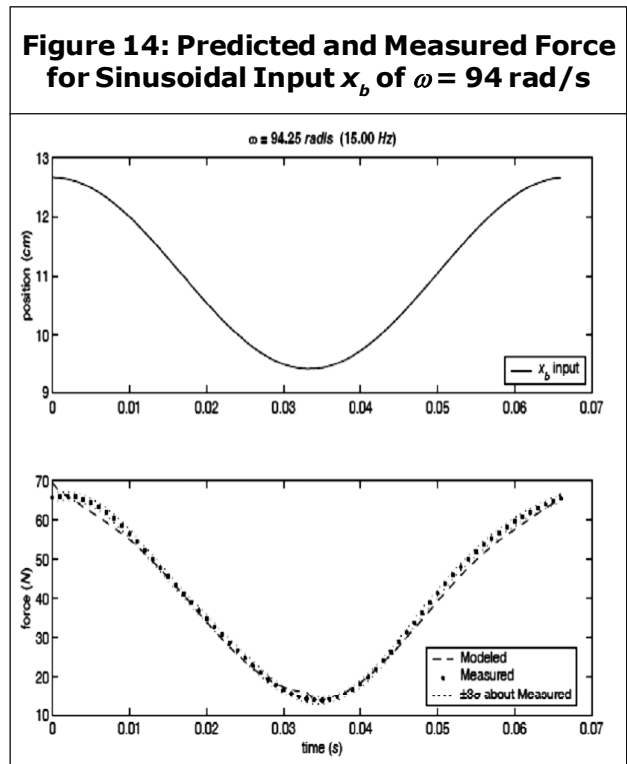
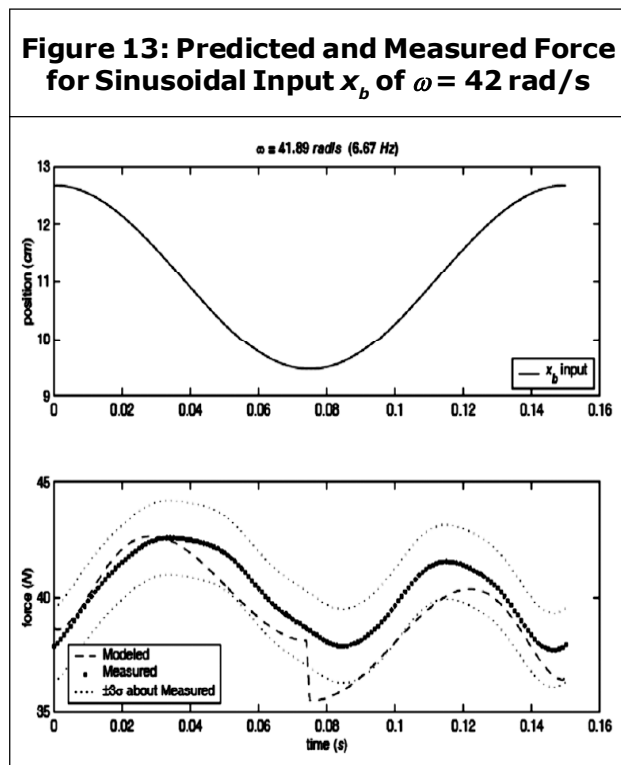
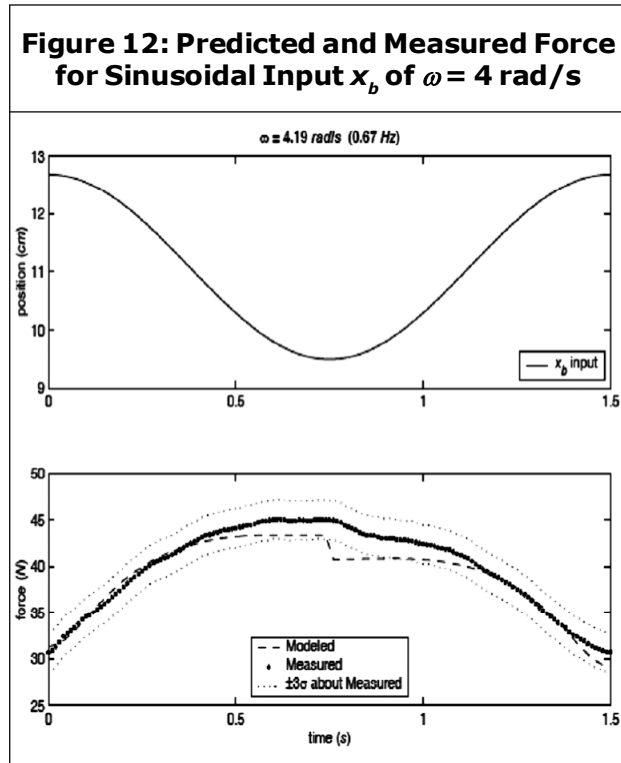
Given a position input  $x_b(t)$ , and all physical parameters correctly defined, the dynamic model predicts the force expected at the constant-force mechanism's output port. A side-by-side comparison of modeled vs. measured force from an actual mechanism shows that the model predicts the dynamic response of the test mechanism quite satisfactorily.

## Modeled vs. Measured Force

Figures 12 to 14 show position and force plots of three dynamic tests of increasing frequency,  $\omega$ . For each figure, the predicted force cycle is calculated directly from the input sinusoid cycle  $x_b$  shown in the position plot, using the dynamic model equations. The measured force cycle in each figure is the result of force data processed as described in Section Dynamic Data Processing. The measured data is banded by  $\pm 3$  pooled sample standard deviations, or  $\pm 3 \sigma$ , representing the 99.74% confidence interval of the measurement.

While the modeled force does not match the measured force point for point, it does predict the average force, the peak-to-peak force difference, and the general shape of the

force profile at any given frequency. These are important and useful elements to gather from a dynamic analysis of the system.

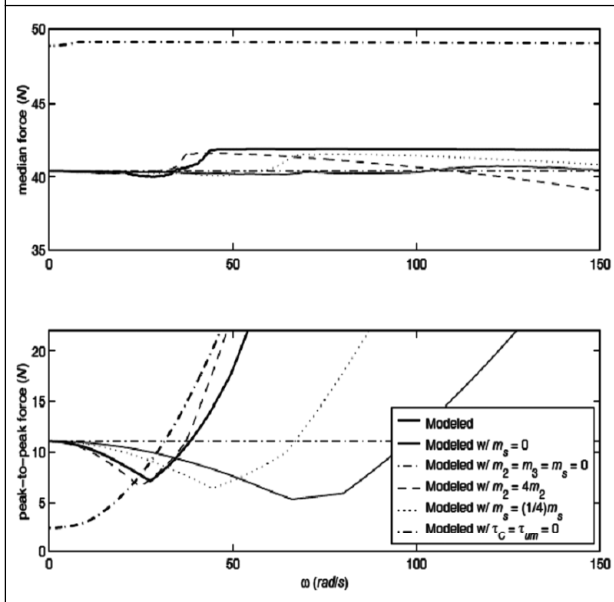


### Dynamic Characterization of the Model

Although nonlinearities make it impossible to express an exact algebraic transfer function for the system, and no simple magnitude and phase plot can be shown, two useful plots can be analyzed. The median force and peak-to-peak force magnitude difference of the dynamic model as functions of frequency are shown in Figure 15. Each frequency assumes a sinusoidal position input with amplitude equal to the full 40% designed mechanism deflection (with a slight “pre-displacement” to give a preload at full expansion). For good plot resolution, the dynamic model response is calculated at 400 separate and equally spaced frequencies.

The heavy solid line represents the force predicted by the dynamic model with all parameters as defined in Table. The next two lines are purely theoretical; what happens

**Figure 15: Frequency Plots Depicting the Median Force and Peak-to-Peak Magnitude Difference Exhibited by the Constant-Force Mechanism**



when the mass of the slider is set to zero, or the mechanism has no inertia at all (all masses set to zero). Setting all the inertias to zero provides a baseline useful for comparison of the other curves, and setting the end mass to zero shows the dynamic response of the constant-force spring isolated as a separate “module”. The fourth and fifth lines in the figure show the effect of multiplying the rigid link mass by four (which represents a possible improvement to the test mechanism, thickening the rigid link to ensure it doesn’t flex), and the effect of reducing the end mass by 75%. Lastly, the modeled force with Coulomb friction  $\tau_c$  and unmodeled torque  $\tau_{um}$  set to zero is given.

Notice that each curve in the peak-to-peak force plot first curves down, then sustains a linear range before it starts to increase (all except for the third curve and last curve). This dip in magnitude difference is demonstrated nicely by Figures 12 to 14. Clearly, the force

profile of Figure 13 at  $\omega = 42$  rad/s has a lower peak-to-peak force difference than the preceding and following figures at  $\omega = 4$  rad/s and  $\omega = 94$  rad/s.

This very interesting and unexpected discovery of the peak-to-peak force plot is that there exists a range of frequencies over which a constant-force mechanism exhibits better constant-force behavior than at static levels. This range of frequencies coincides with the initial magnitude difference drop and most of the linear portion for each of the cases plotted in Figure 15. This unexpected finding significantly improves the likelihood that the compliant constant-force mechanism could be viable in industry.

For instance, if a designer were to use the test mechanism in an application and wanted to output as close to constant-force as possible, he or she would run the mechanism at a frequency of 30 rad/s (see the heavy solid line of Figure 15). This would result in a constant-force mechanism with a median force of 40 N and a force variance of  $\pm 3.5$  N, much better than the  $\pm 6$  N force variance the device demonstrates statically. Or if a designer wanted to maximize the range of frequencies over which the mechanism exhibits “better-than-static” constant-force, he or she could minimize the slider mass as much as possible. Figure 15 shows that the smaller the inertia of the slider, the higher the frequency before the force magnitude difference starts to rise.

Depending on what attributes are most desirable—a wide frequency band with moderately low peak-to-peak force, a single frequency with very low peak-to-peak force, or some other similar effect—the constant-force mechanism parameters can be optimized to

achieve the desired results. It was thought that this better-than-static constant-force phenomenon was caused in part by inclusion of  $\delta C$  and  $\delta um$  in the dynamic model, and the last curve of Figure 15 indicates as much. The peak-to-peak force difference of the dynamic model with  $\tau_C$  and  $\delta um$  set to zero does not manifest a dip over the initial range of frequencies, as do the other curves. Instead, it curves up sharply. However, the phenomenon is not strictly due to  $\tau_C$  and  $\tau_{um}$  only, as evidenced by the third curve of Figure 15. This curve, which represents the dynamic model with all of the inertias set to zero, does include  $\tau_C$  and  $\tau_{um}$ , and it exhibits no dip in peak-to-peak force. So, the phenomenon is likely due to some combination of inertial effects and the effects modeled by  $\tau_C$  and  $\tau_{um}$ . A linearization of the dynamic model about several operating points may hint at the physical reasons for this better-than-static constant-force effect, and may be a fruitful area for further research.

The peak-to-peak force and median force plots end at 150 rad/s for two reasons: (1) most everything of interest in the two plots occurs below this frequency, and (2) there is an upper limit (not necessarily 150 rad/s) above which the constant-force mechanism starts to yield a negative force (i.e., will start to pull instead of push). This occurs when the force cycle exceeds a frequency where the peak-to-peak force equals twice the median force. For the test device (heavy solid line), this occurs at about 99 rad/s.

In few applications will it be useful to give a constant-force mechanism a displacement input by attaching an actuator or surface directly to the slider; the two will usually be touching, but not rigidly connected. When the force

becomes negative, this represents a situation where the slider breaks contact with the actuator or surface, possibly to cause an impact later. Of course these frequencies would be undesirable in most applications and should be avoided.

### Evaluation of the Dynamic Model

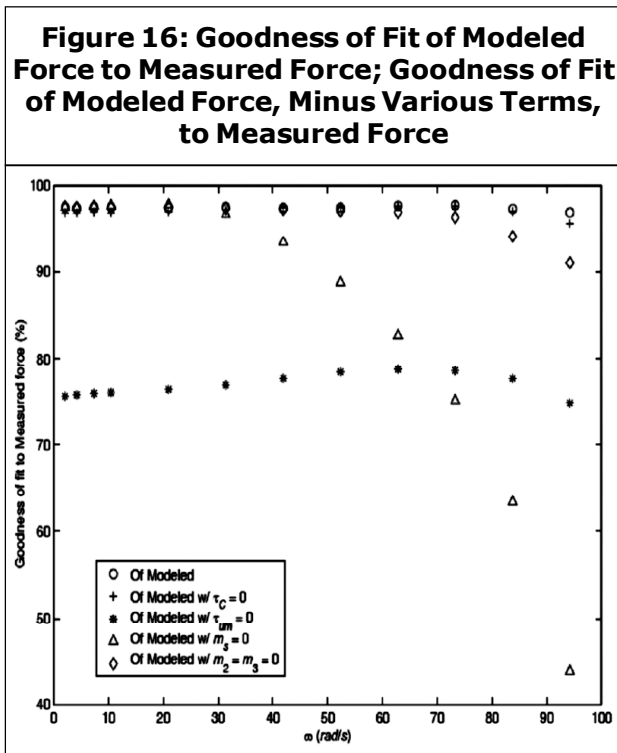
How well does the dynamic model represent the constant-force mechanism? And, if the model anticipates the physical system well, can it be simplified, perhaps by omitting insignificant terms?

Both questions can be answered by analyzing how well the modeled force fits the measured force at each frequency tested. The modeled force is first compared to the measured force with the model untouched. Then various model parameters are set to zero to test their relative importance to the model. As a measure of goodness of fit, the error formula

$$E = \frac{|F_{modeled} - F_{measured}|}{F_{measured}}$$

where  $F_{measured}$  is the average measured force, is applied to each data point in a force cycle and the average error  $E$  over the full force cycle is calculated. For better presentation, goodness of fit  $G_{fit}$  is cast as a percentage,

$G_{fit} = 100(1 - E)$  Figure 16 shows how well the modeled force fits the measured force, for each test frequency. The first plot, represented by small circles, shows the goodness of fit of the dynamic model with all terms intact. The succeeding plots each eliminate one or two model parameters. Even with the complete model, the fit worsens as frequency increases. This is probably due to viscous damping, which was not modeled.



Observe that the dynamic model represents the constant-force mechanism very well. Over the range of frequencies tested, the modeled force is within about 3% relative error of the measured force.

With the first question answered, the second question remains; can the omission of certain minor terms simplify the model? Not surprising is that the worst of these is the model with the end mass set to zero. The end mass possesses most of the system mass upon which inertial forces act. What is surprising is the result of omitting the unmodeled torque term  $\tau_{um}$ . This is interesting compared to the effect of ignoring the Coulomb friction term  $\tau_c$ . The contribution of  $\tau_{um}$  in comparison to  $\tau_c$  is more predominate than anticipated.

Setting the link masses,  $m_2$  and  $m_3$ , to zero represents a fair reduction in the equation of motion for the mechanism, equation. Doing this only sacrifices accuracy at higher

frequencies (see Figure 16), so the dynamic model could be simplified by omitting the link inertias, but removing these terms does not point to a simpler model derivation.

Figure 16 seems to be more useful in illustrating the relative importance of the dynamic model parameters, rather than as a tool to simplify the model.

## CONCLUSION

The constant-force mechanism dynamic model, based on the pseudo-rigid-body model of the mechanism, proves to be a useful, viable abstraction of the physical system. The dynamic model of approximates distributed compliance as a point compliance, while converting the device into a rigid-body mechanism; yet, a dynamic model of the simplified mechanism yields very satisfactory results. This further validates the usefulness of the pseudo-rigid-body model as a dynamics modeling tool, in conjunction with the research of Lyon *et al.* (1997).

Not only does the dynamic model effectively predict the output force of an actual constant-force mechanism, but it illuminates a very useful dynamic property of the mechanism: over certain frequencies it exhibits better constant-force behavior dynamically than statically. The knowledge of such a property makes the constant-force mechanism much more attractive for application in dynamic systems. 

## REFERENCES

1. Ananthasuresh G K and Kota S (1995), "Designing Compliant Mechanisms", *Mechanical Engineering*, Vol. 117, No. 11, pp. 93-96.

2. Atanackovic T M and Cveticanin L J (1996), "Dynamics of Plane Motion of an Elastic Rod", *ASME Journal of Applied Mechanics*, Vol. 63, pp. 392-398.
3. Bahgat B M, Osman M O M and Sankar T S (1981), "An Approach for Dynamic Analysis of Mechanical Systems with Multiple Clearances Using Lagrangian Mechanics", Contributed by the Design Engineering Division of the ASME for Presentation at the Design Engineering Technical Conference, pp. 1-8.
4. Bisshopp K E and Drucker D C (1945), "Large Deflection of Cantilever Beams", *Quarterly of Applied Mathematics*, Vol. 3, No. 3, pp. 272-275.
5. Burns R H and Crossley F R E (1968), "Kinetostatic Synthesis of Flexible Link Mechanisms", ASME Paper No. 68-Mech-36.
6. Darcovich J, Angeles J and Misra A K (1992), "Dynamics of Single-Loop Mechanisms with Flexible Links", *Flexible Mechanisms, Dynamics, and Analysis, DE*, Vol. 47, pp. 453-460.